

# Real-space chirality from crystalline topological defects in the Kitaev spin liquid

Fay Borhani,<sup>1</sup> Arnab Seth,<sup>1</sup> and Itamar Kimchi<sup>1</sup>

<sup>1</sup>*School of Physics, Georgia Institute of Technology, Atlanta, GA 30332, USA*

(Dated: December 6, 2024)

We show that certain crystalline topological defects in the gapless Kitaev honeycomb spin liquid model generate a chirality that depends in a universal manner on their emergent flux. Focusing on 5-7 dislocations as building blocks, consisting of pentagon and heptagon disclinations, we identify the Kitaev bond label configurations that preserve solvability. By defining and computing multiple formulations of local Chern markers we find that the 5 and 7 lattice defects host a contribution to real-space chirality, which we dub “Chern charge” or  $\mathcal{Q}_{\mathcal{M}}$ . The sign of this local Chern charge obeys  $\text{sgn}(\mathcal{Q}_{\mathcal{M}}) = -i \text{sgn}(F)W$  where  $F$  is the disclination Frank angle and  $W = \pm i$  is its emergent-gauge-field flux. We show that lattice curvature and torsion can interplay with the surrounding gapless background to modify the  $\mathcal{Q}_{\mathcal{M}}$  profile and magnitude, but that the sign of  $\mathcal{Q}_{\mathcal{M}}$  is set by local properties of the defect, enabling the identification of Chern charges.

## INTRODUCTION

In the paradigmatic Kitaev model of a quantum spin liquid (QSL) on the 2D honeycomb lattice, it has been known since Kitaev’s original work [1] that plaquettes with an odd number of sides carry an imaginary unit of flux  $W = \pm i$  of the emergent gauge field, which therefore breaks time-reversal (TR) symmetry. This feature of imaginary fluxes (equivalently denoted as  $\pm\pi/2$ -flux) has been shown on various decorated lattices, e.g. the honeycomb lattice with sites replaced by triangles [2]. Recently this feature has also been studied on amorphous lattices in two works [3, 4] and was found to produce a chiral QSL. This non-Abelian chiral QSL is a sought-after phase with a quantized thermal Hall conductance which would be quite interesting to produce in Kitaev materials at zero applied magnetic field. However, since Kitaev materials are spin-1/2 magnetic insulators on the honeycomb lattice, far from any noncrystalline amorphous limit, it is not a priori clear how to apply the above results on chiral QSLs to usual Kitaev materials.

Here we study the chirality and associated thermal Hall conductance arising from odd sided plaquettes in a complementary viewpoint that is more relevant for the honeycomb lattice of Kitaev materials. We consider the fundamental honeycomb lattice defect building blocks that if proliferated would lead to an amorphous lattice without translation symmetry, in particular the honeycomb lattice fundamental 5-7 edge dislocation defect. Kitaev materials hosting spin-1/2 moments on the honeycomb lattice necessarily have such honeycomb lattice dislocations. It is thus necessary to consider the effects of dislocations on the Kitaev QSL in order to correctly analyze experimental data on Kitaev materials. However, the chirality of chiral QSLs (which can be defined by their thermal Hall conductance) is a global topological property of the phase, usually associated with a Chern number of gapped Majorana bands in momentum space, and there is not yet a theory describing chirality effects of isolated dislocation defects in Kitaev materials. In this work we use

the Local Marker described below to compute contributions to the thermal Hall conductance in Kitaev systems with isolated dislocations. This computation allows us to extract a measure of a local chirality contributed by each disclination part of a dislocation. We find that the sign of this local chirality contribution is robustly determined by the defect Frank angle and the emergent flux (Eqn. 1). This computational extraction of the chirality contributed by each defect building block can enable a microscopic understanding of the possible formation of a chiral QSL with quantized thermal Hall effect relevant for Kitaev materials with dislocation defects.

Dislocations in QSLs have often been studied by focusing on their braiding statistics as “twist defects” or “genons” [5, 6], which are helpful if the positions of individual dislocations could be controlled independently and coherently. Dislocations have also been studied as a source of lattice torsion, equivalently a dipole source of lattice curvature (since a basic edge dislocation is a dipole of disclinations with opposite Frank angles), including on the honeycomb lattice of graphene [7]. Here we consider a different effect, studying how quenched dislocations can modify the quantum state in Kitaev materials beyond the conventional non-QSL effects of lattice curvature. This viewpoint was also taken by a prior study of dislocations in the gapped phase of Kitaev’s model, created by a large bond strength anisotropy, which protects unpaired majorana modes on dislocations [8]. The prior study did not consider chirality generation from dislocations, and indeed the lack of global chirality generation is consistent with the strong-anisotropy trivial gap. In contrast, here we consider adding dislocations to the gapless phase of the Kitaev model, where local chirality generation can have important physical effects. The gapless Kitaev model, which occurs when the three types of Kitaev exchanges (x,y,z) all have approximately the same energy scale, is the model that is thought to arise (with perturbations) in most Kitaev materials. It is thus necessary to consider possible chirality effects from defects when investigating Kitaev materials. Finally we note two

recent manuscripts studying the Kitaev gapless QSL on hyperbolic space with homogenous curvature [9, 10]. The artificial hyperbolic-space limit was found to remain gapless. In contrast, below we find that a nonzero local gap is generated by the isolated dislocation defects which are relevant to honeycomb Kitaev materials.

Many potential realizations of the Kitaev model Hamiltonian in magnetic insulators have been discussed in the literature, and the field is well reviewed elsewhere [11–16]. In certain materials even weak Kitaev exchanges have been robustly characterized, such as  $\text{CrI}_3$  [17] and  $\text{YCOB-Cl}$  [18], suggesting the Jackeli-Khaliullin mechanism [19] for generating Kitaev type exchanges can be quite robust. Regarding dislocations, as far as we are currently aware, dislocation defects have not been well characterized in any Kitaev material to date. However such defects always arise in solids. Characterization of other types of defects have been performed for certain Kitaev materials such  $\text{H}_3\text{Li}_2\text{IrO}_6$  [20–22]. Regarding experimental probes of a chiral spin liquid, the theoretical golden standard is quantized  $\kappa_{xy}/T$  thermal Hall conductance. Though experimentally complex it has been increasingly used as a probe in Kitaev materials such as  $\text{RuCl}_3$  and  $\text{Na}_2\text{Co}_2\text{TeO}_6$  [23–26]. Chirality can also be measured locally via scanning magnetometry probes such as with Nitrogen-Vacancy (NV) centers. Usually, both topological and trivial chirality contributions to thermal Hall conductance arise in applied magnetic fields; the possibility of observing chirality from dislocations in the absence of any magnetic fields would therefore be quite remarkable.

The time-reversal-breaking chirality and associated quantized thermal Hall conductance of the chiral QSL has a conventional theoretical description in terms of the Chern number. Recall that for 2D electron systems with conserved charge, the Chern number of the gapped electronic band structure determines the quantized Hall conductance. For the Kitaev QSL the electrons are insulating and their spins fractionalize into majorana fermions without  $U(1)$  symmetry, so the Chern number of the majorana bands determines the thermal Hall conductance [1]. In systems with open boundaries, this quantization is also reflected in neutral chiral edge modes with a bulk-boundary correspondence that still enables band structure methodology. However, the presence of defects prevents the use of momentum-space band-structure methods such as the Chern number. A real space theoretical probe of chirality is thus needed.

Such a set of real-space theoretical probes of chirality have been under development in recent years, due to seminal work by Kitaev [1] and Bianco and Resta [27], often going by the name of “local Chern markers” [1, 27, 28]. These theoretical probes or “markers” are useful in that when they are measured in translationally invariant systems, they exactly reproduce the conventional Chern number. Their definition persists with

disorder, for example disorder averaging a fully gapped but inhomogenous system reproduces the Chern number uniformly across all local markers [27–29]. Local markers can also be defined for 2D interacting systems in terms of Green’s functions [29] and for topological invariants in other dimensions [30]. Other methods exist for measuring the global topology of an inhomogenous system, such as Kitaev’s ABC construction [1] and the Bott index [31], which were also used to compute the nonzero chirality of the Kitaev QSL in homogeneous hyperbolic space [9, 10]. However, the local Chern markers are advantageous in giving real space resolution. Such real space resolution becomes especially important for systems where the gap is only local [32], an issue which arises in the present case of dislocations embedded in an otherwise gapless background, as we discuss below.

## RESULTS

### Summary of results

In this work we investigate the chirality contribution of isolated 5-7 dislocations in Kitaev’s model. By defining Kitaev bond label configurations that preserve exact solvability even in the presence of dislocations (Figure 1 c,d,e), we diagonalize the idealized Kitaev models in the presence of various dislocations and study the resulting states. The local Chern marker is computed to investigate the contributions of such isolated defects to the chirality of the system. We find that these computational results can be naturally interpreted in terms of a “Chern charge” contributed by each 5/7 disclination building block, whose sign is determined by the disclination Frank angle and the emergent flux. (Recall that the Frank angle is the topological invariant of a disclination, measuring the angle subtended by a wedge that is required to be added or removed from the pristine lattice to create the disclination.) In particular, we numerically demonstrate that the sign of the net chirality breaking around each 5 or 7 disclination can be expressed as:

$$\text{sgn}(\mathcal{Q}_{\mathcal{M}}) = -i \text{sgn}(F)W \quad (1)$$

where  $\mathcal{Q}_{\mathcal{M}}$  captures the net TR breaking effect due to the defects,  $W$  and  $F$  are the emergent-gauge-field magnetic flux and the Frank angle of the disclination, respectively. ( $\text{sgn}(F) = 1(-1)$  for a 5(7) disclination respectively.) We dub  $\mathcal{Q}_{\mathcal{M}}$  as *Chern charge*, which creates a local Chern marker field around the defect, in a similar fashion as the electrical charges do in electrostatics (Figure 1 a,b). Using such charge assignment profile, we show that modifying the flux of the disclination, the topology of the magnetic sector can be altered, creating various multipolar configurations analogous to electrostatics.

A central subtlety of isolated defects is that the system remains nearly gapless. However, we show that the essential content of Equation 1 can be extracted by tracking

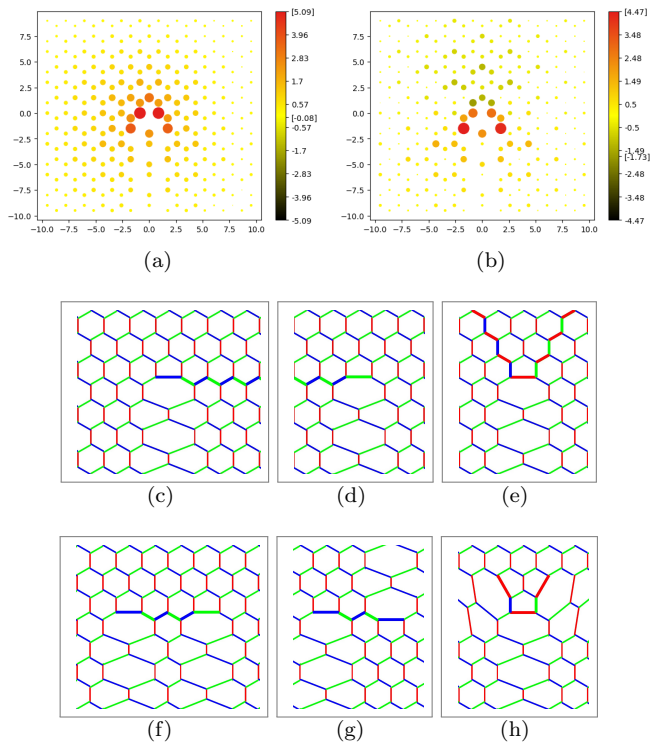


FIG. 1. **5-7 Dislocations in the Kitaev honeycomb model and their contribution to chirality:** (a,b) Pentagon-heptagon (5-7) dislocations, and the  $M_1$  local Chern marker pattern they generate, for the case where (5,7) plaquettes carry  $W$  fluxes of  $(+i,-i)$  (a) and  $(-i,-i)$  (b) respectively. The local marker patterns can be viewed as arising from a monopole (a) and dipole (b) of “Chern charges”  $\mathcal{Q}_M$  associated with the defect fluxes.  $M_1$  on each site is shown as area- $|M_1|$  disk; note  $|M_1|$  is largest near the dislocation core and decays away from it. Max/min  $M_1$  values are shown in brackets on color scale, and are unequal in (b), implying that the  $\pm$  charges  $\mathcal{Q}_M$  assigned to (b) should have unequal magnitude. (c,d,e) Dislocation with Kitaev bond labels that preserve exact solvability. (f,g,h) For multiple dislocations, the flipped-handedness strings of (c,d,e) can be truncated under certain conditions as described in the text. Note that while each dislocation is drawn on flat space with a “tail”, this is only a visualization: all lattice bonds have uniform  $J_K$  regardless of depicted bond length.

a local contribution. We confirm this using perturbation theory and superlattice Chern number computations on a pseudo-dislocation non-topological local defect (Figure 2). We also explore the beyond-local magnitude effects that do depend on curvature and torsion (Figures 3 and 4).

### Solvability of Kitaev models with dislocations

The Kitaev model on the honeycomb lattice [1] is

$$H = J_K \sum_{\langle ij \rangle} \sigma_i^{\alpha_{ij}} \sigma_j^{\alpha_{ij}} \quad (2)$$

where  $\alpha_{ij} = x, y, z$  denotes the three axes, shown in Fig. 1 as bond colors red, green, blue. We consider uniform  $J_K$  on all bonds even in the presence of defects. (This is true even though our drawings of dislocations on the flat 2D plane involves a sequence of stretched bonds; these bonds are identical to any other bond on the lattice.)

The model and its possible realizations are well reviewed elsewhere [11, 13–16]. Here we briefly review its solution in order to introduce relevant notation. The model can be solved via Kitaev’s prescription of decomposing spins in terms of Majorana fermions:  $\sigma_i^\alpha = ib_i^\alpha c_i$  where  $b_i^\alpha$  and  $c_i$  are Majorana fermions sitting at the lattice site  $i$ . The above Hamiltonian can then be rewritten as  $H = (-i/2) \sum_{i,j} J_K u_{ij} c_i c_j$  where,  $u_{ij} = ib_i^{\alpha_{ij}} b_j^{\alpha_{ij}}$  describes  $Z_2$  gauge field residing on the bonds of the honeycomb lattice. Since  $[H, u_{i,\alpha}] = 0$ , the gauge field behaves as a static background field, giving rise to exact solvability of the model. For each closed path the gauge field gives a flux  $W_\circ = \prod_{i\alpha \in \circ} u_{i,\alpha}$  (defined with counterclockwise orientation) which is gauge invariant and conserved. Note that  $W_\circ^2 = 1$  ( $-1$ ) on the even (odd) sided plaquettes respectively. This constraint enforces TR symmetric  $\pm 1$  flux (equivalently denoted by its phase as  $0-$  and  $\pi$ -flux) in the even sided plaquettes, and TR breaking  $\pm i$  flux (equivalently  $\pm\pi/2$ -flux) on the odd sided plaquettes.

In presence of the dislocation, the honeycomb lattice remains three fold coordinated. Certain 3-coloring configurations that preserve solvability can still be defined, as shown in Fig. 1 (c,d,e), where (c) and the related (d) were also found in Ref [8] while (e) is new. Importantly, a dislocation involves an infinite string of sites which have modified Kitaev bond labels relative to the rest of the lattice. These strings also show flipped handedness of  $x, y, z$  labels on the bonds around each site. The choice of the string of flipped handedness (SFH) is associated with the choice of color of the 5-7 bond at the dislocation core, as shown in Fig. 1(c), (d) and (e). String reorientations are related by subsystem symmetry transformations (cycling the bond labels along certain 1D paths). Note that in (c,d) the infinite SFH has a starting point while in (e) it is infinite on both directions.

For lattices with multiple dislocations, in certain configurations the strings can be chosen to be finite. A necessary condition is that the dislocations can be grouped into groups of two or three dislocations with each group having its Burgers vector either vanishing (Fig. 1 (g,h)), or taking a value twice of the Burgers vector of a fundamental 5-7 dislocation, i.e. two dislocations that have parallel Burgers vectors (Fig. 1 (f)). (Recall that the Burgers vector is the topological invariant of a dislocation, measured by the mismatch of the starting and ending point, relative to the pristine lattice, of closed paths that encircle the defect.) An additional condition is that the dislocation positions align so that the strings can overlap; this can be fairly nontrivial as depicted in

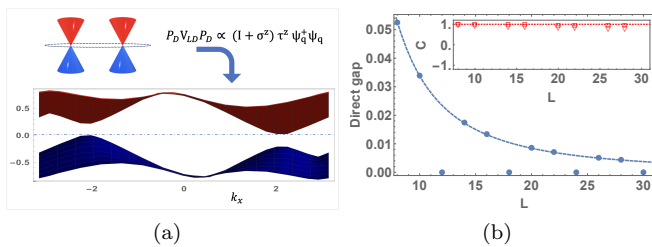


FIG. 2. **Chern number  $C = 1$  generated by periodic array of pseudo-dislocation non-topological local defect and interpretation via perturbation theory:** (a) A periodic array of pseudo-dislocation non-topological local defect  $V_{LD}$  with zero lattice curvature adds a perturbation that opens a direct gap in each Dirac cone, while also preserving a zero-energy eigenvalue in each cone, thanks to the matrix  $(1 + \sigma^z)$  that arises when  $V_{LD}$  is projected to the low energy Dirac cones. Bottom panel: band structure for an array with  $V_{LD}$  defect density of  $1/16$  is here plotted as a function of  $k_x$ , viewed along  $k_y$ , to show the nonzero direct gap and barely vanishing indirect gap. (b) Computations for periodic array with one  $V_{LD}$  defect per unit cell with  $L^2$  sites, at  $\lambda = 1$ . The direct gap ( $\approx 3.38L^{-2}$ , blue dashed line) remains nonzero for  $L \neq 6Z$  (i.e. when the  $K_1, K_2$  cones are not both folded to  $k = 0$ ), allowing a computation of Chern number of the lower band. Note that the fluxes corresponding to  $V_{LD}$  are  $[i, -i]$  on  $[5, 7]$  respectively, so based on the local markers and Eqn. 1 this is expected to behave as an array of purely positive Chern charges  $\mathcal{Q}_M$ . Inset: Indeed, computing the Chern number for the  $L \neq 6Z$  arrays with increasing accuracy (triangle and square symbols), we find that it converges to  $C = 1$  (dotted line). Thus the local effects of dislocations are sufficient to generate a nonzero Chern number, and can be understood within perturbation theory, with a sign predicted by Eqn. 1.

(Fig. 1 (h)). We note that the finite-SFH requirement of total Burgers vector being zero or twice the vector of a single dislocation is quite general and allows for various coarse grained torsion patterns.

### Single dislocations

To motivate the computations of chirality and Chern number which we will turn to in the following sections, we begin with a local Chern marker  $M_1$  computation shown in Fig. 1 (a), (b). This local marker is a measure of chirality in that when computed in translationally invariant systems it reproduces the Chern number. (We discuss its definition and application to defects further below.) Fig. 1 (a), (b) show that each dislocation generates a pattern of  $M_1$  with substantial nonzero magnitude near the dislocation core. This pattern can be interpreted as arising from a Chern charge associated with each disclination, whose sign depends on the flux in accordance with Eqn. 1.

For a single dislocation, the opposite-fluxes configuration is its ground state. This corresponds to Chern charges of equal sign, giving a “monopole” local Chern marker contribution, Fig. 1. The gap from the opposite-fluxes ground state of a dislocation to the the excited

state of uniform-fluxes configuration is approximately  $\Delta_{\text{uniform-fluxes}} \approx 0.038J_K$ .

Since odd-sided plaquettes also carry curvature, a natural question is whether the role of this curvature in setting the chirality is significant or not. A second question is how to relate the local Chern markers  $M_1$  and  $M_2$  (discussed below) to the traditional Chern number defined for periodic lattices, given that a unit cell with nonzero net Burgers vector cannot have the 2D translational symmetry necessary for defining the conventional Chern number.

### Isolating contributions to Chern number from time-reversal breaking local perturbations

In this section we address both of these questions by defining a pseudo-dislocation nontopological local defect  $V_{LD}$  that does not carry curvature. We show that its 2D arrays produce nonzero Chern number with an appropriate sign corresponding to Eqn. 1. We also show how this can be understood within perturbation theory on a dislocation. The results show that the sign of chirality generation arises from purely local perturbation  $V_{LD}$ . In the next section we will argue that, in contrast, the magnitude does involve beyond-local effects related to the pattern of curvatures.

Let us begin by defining a perturbative point of view to describe a dislocation. We note that dislocations, being inherently non-local, cannot be described as a local perturbation to the pristine honeycomb lattice. However, we show that their effects on the magnetic sector can be closely mimicked by introducing a single second nearest neighbor bond violating the bipartiteness of the lattice. The Kitaev model with such a local pseudo-dislocation is obtained by adding the following perturbation:

$$V_{LD} = i\lambda c_{R,\mu} c_{R+d_1,\mu} + \text{h.c.} \quad (3)$$

where  $R$  is the position of the pseudo-dislocation,  $d_1$  is a lattice vector,  $\mu$  is one of the two sublattice indices, and  $\lambda$  is the hopping strength of the second neighbor bond, which we treat as a perturbative parameter. The particular hopping chosen above leads to TR breaking opposite fluxes on the 5- and 7-sided plaquettes around that bond, analogous to Fig. 1 (a).

The above perturbation, being local, is not diagonal in the momentum basis. To the leading order in  $\lambda$ , it generates matrix elements between two sublattices of the Dirac cones. We use a notation such that the low energy theory of the Majorana fermions is rewritten as complex Dirac fermions. This double counts states, which is easily fixed by a factor of 2 when computing total energies, i.e. the complex fermions have hopping  $J_K$ . This gives a Hamiltonian which when projected to the Dirac cones reads  $P_D H P_D = v_F \sum_q \psi_q^\dagger (q_x \sigma^x + q_y \tau^z \sigma^y) \psi_q$ . Here  $v_F = 3J_K/2$ ,  $\sigma$  and  $\tau$  denote the sublattices and valleys, respectively,  $P_D$  is the projector onto the low energy Dirac cones, and  $\psi_q = (c_{K_1+q,A} c_{K_1+q,B} c_{K_2+q,A} c_{K_2+q,B})^T$

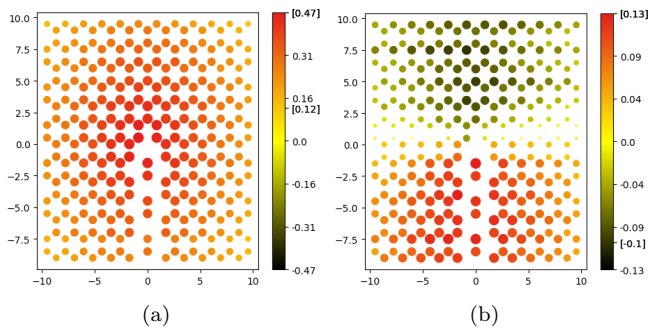


FIG. 3. Variant  $M_2$  local Chern markers, computed for the same flux patterns on a dislocation as in Fig. 1, namely  $(+i,-i)$  and  $(-i,-i)$  for (a), (b) respectively. Here  $M_2(R)$  is plotted for each region  $R$  as a disk of area  $|M_2|$  at site  $r$  below and left of  $R$ . Note that the magnitude and decay profile differ from  $M_1$ , due to the defect curvatures and gapless background, while the structure of Chern charge signs Eqn. 1 remains the same.

with  $K_1$  and  $K_2$  denoting the two Dirac cones. In this notation, the local pseudo-dislocation perturbation leads to an effective low-energy Hamiltonian of the form

$$P_D V_{LD} P_D = \frac{\sqrt{3}\lambda}{2\mathcal{N}} \psi_q^\dagger (I + \sigma^z) \tau^z \psi_q \quad (4)$$

where  $\mathcal{N}$  denotes the total number of unit cells. The first term breaks the inversion symmetry giving rise to tilt in the band structure (see Fig. 2(a)). The second term,  $\sigma^z \tau^z$ , breaks time-reversal and generates a topological mass term for the Dirac cones. This is the central feature of the magnetic physics in presence of a true 5-7 dislocation. Both tilt and splitting grow linearly with  $\lambda$ . However, we note that since there is no non-bipartite coupling for the sublattice not chosen by  $\mu$ , this sublattice exactly preserves the zero energy states, leading to zero gap in the many particle eigenstates.

The nonzero Chern number that results from this topological mass term is seen explicitly in our numerical studies of  $V_{LD}$  periodic arrays, Fig. 2(b). Note the tilt between the two Dirac cones, and the single particle gap which remains nonzero throughout the Brillouin zone, despite the zero energy eigenvalues, thus enabling the rigorous definition of Chern number, which is found to be  $C = +1$ . This array corresponds to an array of the  $(+i,-i)$  dislocation of Fig. 1(a), restricted to only local effects of the dislocation with no curvature. Thus the positive  $M_1$  generated by the dislocation of Fig. 1(a) can be fully captured by the purely local effects of the dislocation, and it indeed results in nonzero positive Chern number.

### Local Marker variants and beyond-local effects from curvatures and gapless background

There are presently multiple competing formulations of local Chern markers, which agree for a uniformly

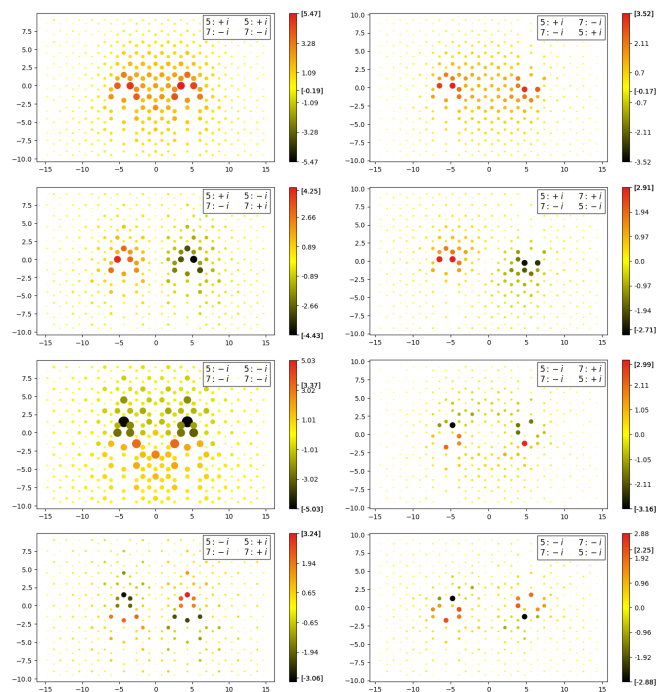


FIG. 4. For two dislocations, aligned versus anti-aligned Burgers vectors (left and right columns respectively) yield different  $M_1$  local markers configurations, suggesting that curvature can have beyond-local effects on the chirality contribution. Insets show the fluxes on the 5 and 7 plaquettes corresponding to their spatial positions.

gapped bulk system, but can differ in the presence of inhomogeneities and boundaries, which are necessarily involved for certain configurations of dislocations. In Figs. 1 and 4 we plot one variant of the local Chern marker, which we call  $M_1$ , which we introduce here through a modification of the  $M_{2011}$  marker that is better at handling open boundaries.  $M_{2011}$  is defined as  $M_{2011}(r) = 4\pi \text{Im}\langle r | P x P y P | r \rangle$  where  $P$  is projection to occupied states. We extend  $M_{2011}$  by defining a marker  $M_1$  as

$$M_1(r) = 4\pi \text{Im}\langle r | P x_b P y_b P | r \rangle ; x_b = L^{-1} \sum_{R \in \text{bulk}} \theta_{x;R} \quad (5)$$

and similarly for  $y_b$ . Here  $\theta_{y;R}$  is the step function on the upper half plane above a point  $R$ , namely  $\theta_{y;R}$  is 1 above  $R$  and 0 below;  $\theta_{x;R}$  follows the analogous definition. The operators  $x_b, y_b$  can be physically interpreted as position operators  $x, y$  whose eigenvalues saturate when approaching the boundaries. This also determines the normalization  $L^{-1}$  of the  $\sum_R$  sum. The particular definition of “bulk” used in the computations is described in the Methods section. Such separations between bulk and boundary have been previously discussed in the literature for local marker and interacting local markers [28, 29].

In order to identify the limitations of the local marker

methodology for the present case, with inhomogeneities and a nearly gapless background, we compare our computation of the marker  $M_1$  to an alternative local marker formulation,  $M_2$ . We define  $M_2$  in close analogy with the 2022 local marker formulation  $M_{2022}$  of D’Ornellas, Barnett and Lee [28]. They begin with a cross-hair at  $R$  giving a contribution map  $C_2(r)$  by  $C_2(r, R) = 4\pi\text{Im}\langle r|P\theta_{x;R}P\theta_{y;R}P|r\rangle$ . Here the step functions  $\theta_{x,y;R}$  have a physical interpretation as the electric potential and the orthogonal flow of charges that together define Hall conductance. Then  $M_{2022}(R) = \sum_{r \in \text{bulk}} C_2(r, R)$ , where the sum over sites  $r$  is restricted to sites in the bulk. Note that in contrast, the 2011 marker  $M_{2011}$  is a sum over all crosshairs  $R$ , as  $M_{2011}(r) = \sum_R C_2(r, R)$ . We define  $M_2$  in analogy to  $M_{2022}$ ,

$$M_2(R) = \sum_{r \in \text{bulk}} 4\pi\text{Im}\langle r|P\theta_{x;R}P\theta_{y;R}P|r\rangle \quad (6)$$

except that we find that the bulk sum over  $r$  is more sensitive to boundary effects compared to the  $R$  bulk sum in  $M_1$ , and thus needs a further restriction; and that given this  $r$  restriction,  $R$  must be restricted even further. Details on these restrictions are given in the Methods section.

The  $M_2$  results for a single dislocation are shown in Fig. 3. Note that the decay profile appears quite different than that of  $M_1$ , and in particular the dipole marker pattern of Fig. 3(b) is quite extended. However, though the relative magnitudes and decay profile is modified compared to  $M_1$ , the monopole and dipole sign structure remains identical between  $M_1$  and  $M_2$ .

To identify the physical origin for this difference between the local marker results, we proceed to consider pairs of nearby dislocations and compute the local marker  $M_1$  they generate. Results are shown in Fig. 4. Two things become evident. First, the magnitude of the local marker generated by each disclination depends sensitively on the curvature profile of nearby space. Recall that each dislocation can be viewed as a dipole of opposite curvatures. Whether the dislocations have their Burgers vectors, and correspondingly their curvature dipole vectors, aligned (Fig. 4 left column) or anti-aligned (right column) greatly impacts the magnitude and profile of the local markers. Second, and in contrast, the pattern of signs of local markers remains invariant, and obeys Eqn. 1.

## DISCUSSION

In this work we introduce the notion of Chern charge  $\mathcal{Q}_{\mathcal{M}}$  to capture the results of local marker computations near 5-7 dislocations of the Kitaev model. We find that each disclination contributes to the local marker with a sign that is determined by its Frank angle (curvature) and by its flux. This result holds unambiguously even

across different formulations of the local markers  $M_1, M_2$ , and can also be seen to arise perturbatively through local effects as well as manifesting in usual Chern numbers of periodic arrays.

We also find unambiguous evidence that lattice curvature can impact the magnitude of the Chern charge  $\mathcal{Q}_{\mathcal{M}}$ , as in the nonequal dipole pattern of Fig. 1(b) and the patterns of Fig. 4. These results also show that the clean limit’s gapless Majorana fermions are important for a quantitative understanding of the generation of chirality that results from introducing a topological defect. Heuristically, the gapless fermions can carry information about lattice curvature across large length scales. Thus it is clear that any quantitative theory of how curvature controls  $\mathcal{Q}_{\mathcal{M}}$  would depend sensitively on the nature of the surrounding background: gapless, topologically gapped or trivially gapped through anisotropy.

The gapless scenario poses interesting questions. Due to the gapless background, any “edge states” would be extended. It will be interesting to consider how chirality is generated when defects occur at small but finite density [4? ]. It will also be interesting to consider realizations of Kitaev models and the appearance and properties of dislocations, disclinations and other topological defects in those models.

Experimental probes of the effects described above include thermal Hall conductivity and related local probes of chirality such as NV-center magnetometry. Identifying a local chirality contribution near dislocation cores at zero applied magnetic field would give strong evidence of a Kitaev-model origin, as opposed to conventional sources of thermal Hall conductivity that can arise in an applied magnetic field.

## METHODS

$M_1$  marker was computed with a sum over “bulk” sites defined as being away from the open boundary at a real space distance  $b$ , with  $b = 5$ . Real space distances are defined with a honeycomb lattice nearest neighbor vector of length 1. Due to the emergent Lorentz symmetry of Dirac cones at low energies, relevant to the Majorana fermions of the gapless Kitaev model, real space distance was found to be a better measure compared to numbers of unit cells.  $M_2$  marker was computed with open boundaries and with a sum over “interior bulk” sites defined as being within a real space region centered at the origin, with square aspect ratio and real space size  $c \times c$ , with  $c = 24$ . This defines the marker  $M_2$  within a smaller square region centered at the origin. Computations were performed with the following system sizes. Here system sizes are given by the number of sites along the zig-zag edge and armchair edge, i.e. twice the number of a four site unit cell, such that the total number of sites is  $L_x L_y$ , and the real space extent is  $\sqrt{3}L_x/2 \times 3L_y/2$ . Fig 1 (a,b):

$(L_x, L_y) = (40, 36)$ . Fig 3:  $(L_x, L_y) = (40, 36)$ . Fig 4:  $(L_x, L_y) = (56, 36)$ . Fig 2 Berry curvature integration was performed to obtain Chern number using  $72 \times 72$  and  $144 \times 144$  mesh grids denoted by triangle and square symbols respectively. Diagonalization of the Majorana spectrum was performed using the python PyBinding package [33].

## ACKNOWLEDGEMENTS

This work was supported by the U.S. Department of Energy Office of Science, Award Number DE-SC0025478.

## DATA AVAILABILITY

The datasets generated and/or analysed during the current study will be available at the Georgia Tech Digital Repository following publication.

## REFERENCES

- 
- [1] A. Kitaev, Anyons in an exactly solved model and beyond, *Annals of Physics* **321**, 2 (2006).
- [2] H. Yao and S. A. Kivelson, Exact chiral spin liquid with non-abelian anyons, *Physical Review Letters* **99**, 247203 (2007).
- [3] G. Cassella, P. D’Ornellas, T. Hodson, W. M. H. Natori, and J. Knolle, An exact chiral amorphous spin liquid, *Nature Commun.* **14**, 6663 (2023), [arXiv:2208.08246 \[cond-mat.str-el\]](#).
- [4] A. G. Grushin and C. Repellin, Amorphous and polycrystalline routes toward a chiral spin liquid, *Physical Review Letters* **130**, 186702 (2023).
- [5] M. Barkeshli, C.-M. Jian, and X.-L. Qi, Twist defects and projective non-Abelian braiding statistics, *Physical Review B* **87**, 045130 (2013).
- [6] B. Yan and S. X. Cui, Generalized Kitaev Spin Liquid model and Emergent Twist Defect, [arXiv:2308.06835 \(2023\)](#), [arXiv:2308.06835 \[cond-mat\]](#).
- [7] M. Vozmediano, M. Katsnelson, and F. Guinea, Gauge fields in graphene, *Physics Reports* **496**, 109 (2010).
- [8] O. Petrova, P. Mellado, and O. Tchernyshyov, Unpaired Majorana modes on dislocations and string defects in Kitaev’s honeycomb model, *Physical Review B* **90**, 134404 (2014).
- [9] F. Duset, T. Hofmann, A. Maity, Y. Iqbal, M. Greiter, and R. Thomale, *Chiral Gapless Spin Liquid in Hyperbolic Space* (2024), [arXiv:2407.15705 \[cond-mat\]](#).
- [10] P. M. Lenggenhager, S. Dey, T. Bzdušek, and J. Maciejko, *Hyperbolic Spin Liquids* (2024), [arXiv:2407.09601 \[cond-mat\]](#).
- [11] L. Savary and L. Balents, Quantum spin liquids: A review, *Reports on Progress in Physics* **80**, 016502 (2016).
- [12] S. M. Winter, A. A. Tsirlin, M. Daghofer, J. van den Brink, Y. Singh, P. Gegenwart, and R. Valentí, Models and materials for generalized Kitaev magnetism, *Journal of Physics: Condensed Matter* **29**, 493002 (2017).
- [13] M. Hermanns, I. Kimchi, and J. Knolle, Physics of the Kitaev Model: Fractionalization, Dynamic Correlations, and Material Connections, *Annual Review of Condensed Matter Physics* **9**, 17 (2018).
- [14] H. Takagi, T. Takayama, G. Jackeli, G. Khaliullin, and S. E. Nagler, Concept and realization of Kitaev quantum spin liquids, *Nature Reviews Physics* **1**, 264 (2019).
- [15] S. Trebst and C. Hickey, Kitaev materials, *Physics Reports Kitaev Materials*, **950**, 1 (2022).
- [16] I. Rousochatzakis, N. B. Perkins, Q. Luo, and H.-Y. Kee, Beyond Kitaev physics in strong spin-orbit coupled magnets, *Reports on Progress in Physics* **87**, 026502 (2024).
- [17] J. Kim, S. Banerjee, J. Kim, M. Lee, S. Son, J. Kim, T. S. Jung, K. I. Sim, J.-G. Park, and J. H. Kim, Spin and lattice dynamics of the two-dimensional van der Waals ferromagnet CrI<sub>3</sub>, *npj Quantum Materials* **9**, 1 (2024).
- [18] A. Seth, J. C. Prestigiacomo, A. Xu, Z. Zeng, T. D. Ford, B. S. Shivaram, S. Li, P. A. Lee, and I. Kimchi, *Disorder-induced spin-cluster ferrimagnetism in a doped kagome spin liquid candidate* (2024), [arXiv:2411.11827](#).
- [19] G. Jackeli and G. Khaliullin, Mott insulators in the strong spin-orbit coupling limit: From heisenberg to a quantum compass and kitaev models, *Physical Review Letters* **102**, 017205 (2009).
- [20] T. Takayama, A. Kato, R. Dinnebier, J. Nuss, H. Kono, L. S. I. Veiga, G. Fabbris, D. Haskel, and H. Takagi, Hyperhoneycomb Iridate beta-Li<sub>2</sub>IrO<sub>3</sub> as a Platform for Kitaev Magnetism, *Physical Review Letters* **114**, 077202 (2015).
- [21] Y.-X. Yang, C.-Y. Jiang, L.-L. Huang, Z.-H. Zhu, C.-S. Chen, Q. Wu, Z.-F. Ding, C. Tan, K.-W. Chen, P. K. Biswas, A. D. Hillier, Y.-G. Shi, C. Liu, L. Wang, F. Ye, J.-W. Mei, and L. Shu, Muon spin relaxation study of spin dynamics on a Kitaev honeycomb material H<sub>3</sub>Li<sub>2</sub>Ir<sub>2</sub>O<sub>6</sub>, *npj Quantum Materials* **9**, 1 (2024).
- [22] T. Halloran, Y. Wang, K. W. Plumb, M. B. Stone, B. Winn, M. K. Graves-Brook, J. A. Rodriguez-Rivera, Y. Qui, P. Chauhan, J. Knolle, R. Moessner, N. P. Armitage, T. Takayama, H. Takagi, and C. Broholm, *Continuum of magnetic excitations in the Kitaev honeycomb iridate D<sub>3</sub>Li<sub>2</sub>Ir<sub>2</sub>O<sub>6</sub>* (2024), [arXiv:2402.08083](#).
- [23] Y. Kasahara, T. Ohnishi, Y. Mizukami, O. Tanaka, S. Ma, K. Sugii, N. Kurita, H. Tanaka, J. Nasu, Y. Motome, T. Shibauchi, and Y. Matsuda, Majorana quantization and half-integer thermal quantum Hall effect in a Kitaev spin liquid, *Nature* **559**, 227 (2018).
- [24] P. Czajka, T. Gao, M. Hirschberger, P. Lampen-Kelley, A. Banerjee, N. Quirk, D. G. Mandrus, S. E. Nagler, and N. P. Ong, Planar thermal Hall effect of topological bosons in the Kitaev magnet  $\alpha$ -RuCl<sub>3</sub>, *Nature Materials* **22**, 36 (2023).
- [25] H. Takeda, J. Mai, M. Akazawa, K. Tamura, J. Yan, K. Moovendaran, K. Raju, R. Sankar, K.-Y. Choi, and M. Yamashita, Planar thermal Hall effects in the Kitaev spin liquid candidate Na<sub>2</sub>Co<sub>2</sub>TeO<sub>6</sub>, *Physical Review Research* **4**, L042035 (2022).
- [26] X. Hong, M. Gillig, W. Yao, L. Janssen, V. Kocsis, S. Gass, Y. Li, A. U. B. Wolter, B. Büchner, and C. Hess, Phonon thermal transport shaped by strong spin-phonon scattering in a Kitaev material Na<sub>2</sub>Co<sub>2</sub>TeO<sub>6</sub>, *npj Quan-*

- [tum Materials](#) **9**, 1 (2024).
- [27] R. Bianco and R. Resta, Mapping topological order in coordinate space, [Physical Review B](#) **84**, 241106 (2011).
- [28] P. d'Ornellas, R. Barnett, and D. K. K. Lee, Quantized bulk conductivity as a local Chern marker, [Physical Review B](#) **106**, 155124 (2022).
- [29] A. A. Markov and A. N. Rubtsov, Local marker for interacting topological insulators, [Physical Review B](#) **104**, L081105 (2021).
- [30] J. D. Hannukainen, M. F. Martínez, J. H. Bardarson, and T. K. Kivornig, Local Topological Markers in Odd Spatial Dimensions and Their Application to Amorphous Topological Matter, [Physical Review Letters](#) **129**, 277601 (2022).
- [31] M. B. Hastings and T. A. Loring, Topological insulators and  $C^*$ -algebras: Theory and numerical practice, [Annals of Physics July 2011 Special Issue](#), **326**, 1699 (2011).
- [32] J. Henheik and T. Wessel, [Response theory for locally gapped systems](#) (2024), [arXiv:2410.10809](#).
- [33] D. Moldovan, M. Andelkovic, and F. Peeters, [Pybinding v0.9.5: A Python package for tight-binding calculations](#), Zenodo (2020).

#### AUTHOR CONTRIBUTIONS

F.B., A.S., and I.K. all contributed to designing the research, writing the code, performing the research, and writing the manuscript.

#### COMPETING INTERESTS

The authors declare no competing interests.